Iterative learning scheme for crystal structure prediction with anharmonic lattice dynamics

Hao Gao [1,2] Yue-Wen Fang [1,*] and Ion Errea [1,2,3,†]

[1] *Centro de Física de Materiales (CFM-MPC), CSIC-UPV/EHU, Manuel de Lardizabal pasealekua 5, 20018 Donostia/San Sebastián, Spain*

[2] *Fisika Aplikatua Saila, Gipuzkoako Ingeniaritza Eskola, University of the Basque Country (UPV/EHU), Europa Plaza 1, 20018 Donostia/San Sebastián, Spain*

[3] *Donostia International Physics Center (DIPC), Manuel de Lardizabal Pasealekua 4, 20018 Donostia/San Sebastián, Spain*

(Received 23 December 2025; revised 12 March 2026; accepted 30 March 2026; published 15 April 2026)

First-principles based crystal structure prediction (CSP) methods have proved to be an essential tool for the discovery of new materials. However, in solids close to displacive phase transitions, which are common in ferroelectrics, thermoelectrics, charge-density wave systems, or superconducting hydrides, the ionic contribution to the free energy and lattice anharmonicity become significant, limiting the capacity of CSP techniques to determine the thermodynamic stability of competing phases. While variational methods like the stochastic self-consistent harmonic approximation (SSCHA) accurately account for anharmonic lattice dynamics *ab initio*, their high computational cost makes them impractical for CSP. Machine-learning interatomic potentials offer accelerated sampling of the energy landscape compared to purely first-principles approaches, but their reliance on extensive training data and limited generalization restricts practical applications. Here, we propose an iterative learning framework combining evolutionary algorithms, atomic foundation models, and SSCHA to enable CSP with anharmonic lattice dynamics. Foundation models enable robust relaxations of random structures, drastically reducing the required training data. Applied to the highly anharmonic H_3S system, our framework achieves good agreement with benchmarks based on density functional theory, accurately predicting phase stability and vibrational properties from 50 to 200 GPa. In PdH, our method is capable of revealing that the true ground state of the system is the rock-salt structure even if classical crystal structure predictions favor the zincblende structure. Importantly, we find that the statistical averaging in the SSCHA reduces the error in the free energy evaluation, avoiding the need for extremely high accuracy of machine-learning potentials. This approach bridges the gap between data efficiency and predictive power, establishing a practical pathway for CSP with anharmonic lattice dynamics.

DOI: 10.1103/fcrd-8zzf

I. INTRODUCTION

Crystal structure prediction (CSP) coupled with density functional theory (DFT) is a fundamental tool for the discovery of novel materials and leads to breakthroughs across diverse domains, including superhard materials, energetic materials, and exotic chemical compounds [1–4]. A noteworthy success of CSP is its application in discovering high-temperature superconducting hydrides [5–12]. Inspired by the progress of CSP in hydrogen-based superconductors, some hydrides such as H_3S [7] and LaH_{10} [8,9] with superconducting critical temperatures beyond 200 K have been experimentally synthesized and confirmed at extreme pressures [13–16].

Despite these successes, a key limitation of conventional CSP is its neglect of quantum and thermal lattice vibrational effects in the energetics. Standard CSP workflows rank candidate structures by enthalpy after relaxation on the Born-Oppenheimer (BO) potential energy surface (PES), ignoring the kinetic energy of the ions to reduce computational costs. However, it breaks down when ionic lattice dynamics, highly influenced by the anharmonic part of the PES, play an important role in the thermodynamic stability, as is the case in systems close to displacive phase transitions such as thermoelectric materials [17–22], ferroelectrics or quantum paraelectrics [23–25], charge-density wave systems [26–29], etc. In all of these cases, CSP methods miss phases stabilized by quantum and thermal ionic fluctuations, given that none of them correspond to a local minimum of the PES.

This limitation is particularly evident in superconducting hydrides, where light hydrogen atoms are subject to strong quantum fluctuations that generate significant anharmonic effects [30–35]. Such anharmonicity substantially modifies free energy surfaces, altering both thermodynamic and dynamical phase stability from the conclusions drawn exclusively from the PES obtained within the BO approximation. For both H_3S and LaH_{10} systems, the experimentally identified cubic phases that yield the highest superconducting critical temperatures [13,14,36] were theoretically predicted to be dynamically unstable at the relevant experimental pressures within the standard harmonic approximation (HA), characterized by imaginary phonon modes and higher BO enthalpies than competing distorted phases. Crucially, incorporation of anharmonic effects eliminates these imaginary modes and stabilizes the cubic structures thermodynamically [31,32], thus making possible the existence of these cubic structures with

*Contact author: yuewen.fang@ehu.eus
†Contact author: ion.errea@ehu.eus

high electron–phonon coupling at lower pressures and raising a critical question of whether anharmonic effects should be incorporated into CSP to discover high superconducting critical temperature (T_c) hydrides at lower pressures. However, efforts to include anharmonic lattice dynamics in CSP remain scarce. Despite Kruglov *et al.* [37] proposing a hybrid approach combining evolutionary algorithms (EA), molecular dynamics (MD), thermodynamic integration technique, and machine-learning interatomic potentials (MLIPs), a generally practical method for CSP that accounts for anharmonic effects is still lacking.

MLIPs are known to accelerate both SSCHA [17,38] and CSP calculations [4,39–47]. The features required from the potentials by these methods are, however, different. SSCHA requires MLIPs with high accuracy in computing atomic forces and energies of structures within a small configuration space, defined by the quantum and thermal fluctuations of a particular compound. On the other hand, CSP requires general, robust, and transferable MLIPs covering most of the configuration space, given that the structures generated during CSP are highly diverse, and specific-purpose MLIPs usually require massive training data to avoid failure in local optimizations for randomly generated structures. Recently, multiple atomic foundation models pretrained on large datasets have been proposed [48–50]. These models enable "robust" MD simulations and geometry optimizations of various systems and random structures without additional training [48–50]. Moreover, fine-tuning with a small amount of system-specific data further enhances their accuracy for target systems [46,50], bridging the gap between data efficiency and predictive power.

Here, we propose an iterative learning scheme that combines EA and atomic foundation models, followed by SSCHA relaxations, with the aim of implementing CSP with anharmonic lattice dynamics. The application of foundation models dramatically reduces the required training data size. Crucially, we reveal that the computation of thermodynamic properties by SSCHA does not require MLIPs with ultrahigh accuracy. Applied to the highly anharmonic H_3S [7,13,30,51] and PdH [33,35] systems, our framework achieves excellent agreement with DFT benchmarks, indicating its potential for practical CSP with anharmonicity.

II. ANHARMONICITY WITHIN THE STOCHASTIC SELF-CONSISTENT HARMONIC APPROXIMATION

Before describing the iterative learning scheme to develop MLIPs accurate enough to perform CSP within the SSCHA, we find it convenient to review the latter theory. The SSCHA [33,52,53] is a variational method used to obtain the structural and vibrational properties of materials at any temperature while explicitly including quantum ionic effects. The approach minimizes a trial free energy $\mathcal{F}[\tilde{\rho}]$, defined as a functional of a trial density matrix $\tilde{\rho}$. According to the Gibbs-Bogoliubov variational principle, the minimum value of $\mathcal{F}[\tilde{\rho}]$ provides an upper bound to the true free energy F of the system,

$$\mathcal{F}[\tilde{\rho}] = \langle K + V \rangle_{\tilde{\rho}} - TS[\tilde{\rho}] \geqslant F. \tag{1}$$

Here, $\langle K + V \rangle_{\tilde{\rho}}$ represents the quantum statistical average of the ionic kinetic energy K and the BO energy V, while the second term accounts for the entropic contribution, with S being the entropy associated with the ions and T the temperature. The notation $\langle O \rangle_{\tilde{\rho}}$ denotes the quantum statistical average of an operator O evaluated using the trial density matrix $\tilde{\rho}$.

The trial density matrix of the SSCHA is approximated as the one described by an auxiliary harmonic Hamiltonian,

$$\mathcal{H}_{\boldsymbol{\mathcal{R}},\boldsymbol{\Phi}} = K + \frac{1}{2}\sum_{ab}(R_a - \mathcal{R}_a)\Phi_{ab}(R_b - \mathcal{R}_b). \tag{2}$$

Here, $\boldsymbol{\mathcal{R}}$ are the centroid positions, which correspond to the average atomic positions, and $\boldsymbol{\Phi}$ the auxiliary force-constant matrix, which determines the amplitude of the fluctuations of the ions around $\boldsymbol{\mathcal{R}}$. $\boldsymbol{R}$ denotes all ionic positions in one single vector, and the indices a and b run over both atomic and Cartesian coordinates (from 1 to $3N_a$, with N_a the number of atoms in the cell). The ionic probability distribution defined by the auxiliary harmonic Hamiltonian is a Gaussian written as

$$\tilde{\rho}_{\boldsymbol{\mathcal{R}},\boldsymbol{\Phi}}(\boldsymbol{R}) = \sqrt{\det(\boldsymbol{\Psi}^{-1}/2\pi)} \times \exp\left[-\frac{1}{2}\sum_{ab}(R_a - \mathcal{R}_a)\Psi_{ab}(R_b - \mathcal{R}_b)\right], \tag{3}$$

where $\boldsymbol{\Psi}$ is the displacement–displacement correlation matrix

$$\Psi_{ab} = \langle u_a u_b \rangle_{\tilde{\rho}_{\boldsymbol{\mathcal{R}},\boldsymbol{\Phi}}}, \tag{4}$$

with displacements $\boldsymbol{u} = \boldsymbol{R} - \boldsymbol{\mathcal{R}}$. Given that the trial density matrix is fully parametrized by the centroid positions $\boldsymbol{\mathcal{R}}$ and the auxiliary force constants $\boldsymbol{\Phi}$, the SSCHA minimizes the

$$\mathcal{F}[\boldsymbol{\mathcal{R}}, \boldsymbol{\Phi}] = \langle K + V \rangle_{\tilde{\rho}_{\boldsymbol{\mathcal{R}},\boldsymbol{\Phi}}} - TS[\tilde{\rho}_{\boldsymbol{\mathcal{R}},\boldsymbol{\Phi}}] \tag{5}$$

functional with respect to these variables. At the end of the minimization, not only a good approximation of the free energy is obtained, but the obtained centroid positions also correspond to the renormalized average positions of the ions considering thermal and quantum ionic fluctuations and anharmonicity. The SSCHA can also effectively relax lattice parameters at any pressure considering lattice anharmonicity [53].

The SSCHA free energy minimization is implemented with a preconditioned gradient-descent algorithm [53], which requires the calculation of the

$$\frac{\partial \mathcal{F}}{\partial \mathcal{R}_a} = -\left\langle \mathrm{f}_a^{\mathrm{BO}}(\boldsymbol{R}) \right\rangle_{\tilde{\rho}_{\boldsymbol{\mathcal{R}},\boldsymbol{\Phi}}} \tag{6}$$

and

$$\mathcal{G}_{ab}^{\boldsymbol{\Phi}} = \left\langle \left(\mathrm{f}_b^{\mathrm{BO}}(\boldsymbol{R}) - \mathrm{f}_b^{\mathcal{H}_{\boldsymbol{\mathcal{R}},\boldsymbol{\Phi}}}(\boldsymbol{R})\right) \sum_e \Psi_{ae}^{-1}(R_e - \mathcal{R}_e) \right\rangle_{\tilde{\rho}_{\boldsymbol{\mathcal{R}},\boldsymbol{\Phi}}} \tag{7}$$

quantum statistical averages. Here, $\mathbf{f}_b^{\mathrm{BO}}(\boldsymbol{R})$ are the Born-Oppenheimer forces on the ions, evaluated either from DFT or an MLIP in this work, while $\mathbf{f}_b^{\mathcal{H}_{\boldsymbol{\mathcal{R}},\boldsymbol{\Phi}}}(\boldsymbol{R})$ are the forces from the auxiliary harmonic Hamiltonian $\mathcal{H}_{\boldsymbol{\mathcal{R}},\boldsymbol{\Phi}}$. These averages

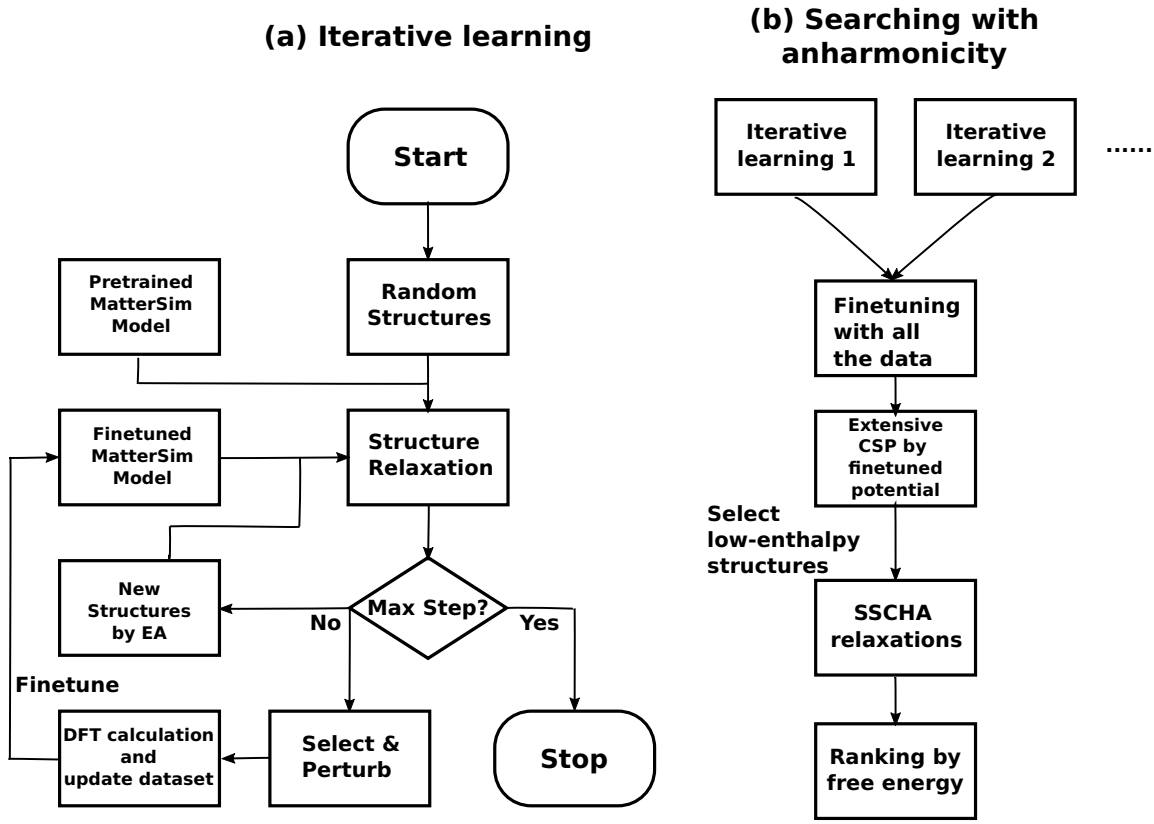

FIG. 1. Iterative learning (a) and SSCHA-assisted searching (b) workflows in this work.

are calculated stochastically as

$$\frac{\partial \mathcal{F}}{\partial \boldsymbol{\mathcal{R}}} = -\frac{1}{N_c}\sum_{i}^{N_c} \mathbf{f}^{\mathrm{BO}}(\boldsymbol{R}_i), \tag{8}$$

and

$$\mathcal{G}^{\boldsymbol{\Phi}}_{ab} = \frac{1}{N_c}\sum_{i}^{N_c} \mathcal{G}^{\boldsymbol{\Phi}}_{i,ab}, \tag{9}$$

where

$$\mathcal{G}^{\boldsymbol{\Phi}}_{i,ab} = \left(\mathrm{f}^{\mathrm{BO}}_b(\boldsymbol{R}_i) - \mathrm{f}^{\mathcal{H}_{\boldsymbol{\mathcal{R}},\boldsymbol{\Phi}}}_b(\boldsymbol{R}_i)\right)\sum_e \Psi^{-1}_{ae}(R_{i,e} - \mathcal{R}_e). \tag{10}$$

The set of ionic configurations $\{\boldsymbol{R}_i\}$ is created according to the Gaussian distribution in Eq. (3). In Eqs. (8) and (9), N_c is the total number of configurations created.

III. CRYSTAL STRUCTURE PREDICTION INCLUDING IONIC ANHARMONICITY WITH MACHINE-LEARNING INTERATOMIC POTENTIALS

A. Iterative learning

The approach proposed in this work focuses on training MLIPs that are both broadly applicable across the entire configuration space as well as accurate enough for further thermodynamic calculations at the anharmonic level of stable and metastable phases defined by a specific set of elements. To meet these requirements, we combine iterative MLIP training with an EA-based CSP, starting from the MatterSim foundation model [50]. Using a robust foundation model as a starting point allows us to relax random crystals at high pressures in a robust manner without an initial fine-tuning. This avoids training MLIPs on random, unrelaxed configurations with high energies, thereby largely reducing the size of the training set and making the sampled structures more physically meaningful. In this sense, the present workflow mainly differs from previous MLIP-assisted CSP methods [39–45] in the preparation of the initial data for iterative training, resulting in a more robust search in practice.

The iterative learning process [Fig. 1(a)] starts with randomly generated structures that are relaxed by the foundation MatterSim model in the first generation. Although MatterSim performs structure relaxations robustly under high pressures, it can still fail to predict phase diagrams correctly, as shown in the following section. To address this issue, several of the obtained local minima are selected for DFT sampling in order to fine-tune the model iteratively and improve its accuracy. Here, we employ simple random selection while retaining duplicates in the population. This strategy increases the chances of selecting low-energy configurations, as they often appear multiple times owing to evolutionary operators and basins of attraction on the PES during EA-based searching. Random distortions are applied to the atomic positions and cell parameters of the selected configurations to generate structures for single-point DFT calculations. The DFT energies, forces, and stresses obtained for them are used to update the dataset. Because training large models on full historical data is computationally demanding, the updated dataset is formed by combining the new DFT data from the current generation with a random subset of the previous dataset. This

combined dataset is then split into training, validation, and test sets, and MatterSim is fine-tuned on it. In parallel, new structures are generated by EA and relaxed using the fine-tuned MatterSim model, which are passed to the next generation. This search-and-learn cycle continues until a predefined maximum number of iterations is reached [Fig. 1(a)]. If the target accuracy of the potential is not obtained, further cycles are performed. This iterative learning is implemented [Fig. 1(a)] in the MAGUS (Machine Learning and Graph Theory Assisted Universal Structure Searcher) code [42,54,55].

B. SSCHA-assisted crystal structure searching

During each iterative learning process, the target pressure is fixed. To extend the configuration space covered by generated datasets, multiple iterative learning processes could be carried out at different pressures, as shown in Fig. 1(b). The MatterSim model is then retrained on the combined dataset using the pretrained model as the starting point. The resulting well-trained MatterSim potential enables subsequent EA-based CSP searches with more generations for larger systems in a wide range of pressures, as well as accurate SSCHA relaxations of the generated structures in the CSP trajectory. In fact, once the potential is fine-tuned and acquires the desired accuracy, extensive CSP searches are performed at different pressures. In order to perform CSP at the anharmonic level, several low-enthalpy structures are selected and SSCHA relaxations are performed for them to obtain their free energies and rank their relative stabilities, as shown in Fig. 1(b). The SSCHA calculations can be performed at any temperature, starting from zero kelvin, effectively enabling finite-temperature crystal structure predictions.

IV. COMPUTATIONAL DETAILS

A. Crystal structure prediction and iterative learning details

1. H_3S

We first test the proposed approach on superconducting hydride H_3S [7,13,30,51] which is well known as a highly anharmonic system. Initially, two independent iterative learning and searching processes are performed at 75 and 125 GPa, starting from the MatterSim foundation model with nearly one million parameters (the model named "MatterSim-v1.0.0-1M" in MatterSim repository [56]). The number of atoms in the structures ranges from 4 to 32. Each search consists of 10 generations of the iterative learning process [Fig. 1(a)], with 1000 structures relaxed per generation. Among them, 900 are randomly generated and 100 are produced by evolution operators, except for the first generation, in which all the structures are randomly generated. After relaxations, 10 structures are sampled randomly, and each undergoes 10 different distortions: atomic positions shift by 0.05 Å in random directions, while random strains from –5% to 5% are applied to cells. This step creates 100 distorted structures per generation for single-point DFT calculations. In addition to the newly computed DFT dataset, 100 configurations are randomly sampled from the previous training set, leading to 200 configurations used for fine-tuning. They are then divided into training, validation, and test sets in an 8:1:1 ratio. The MatterSim model is fine-tuned for 50 epochs with a learning rate of 2×10^{-4} in each generation.

Datasets from both searches are combined to fine-tune the final MatterSim foundation model, as shown in Fig. 1(b). The final training, validation, and test datasets contain 1600, 200, and 200 configurations, respectively. The foundation model is firstly fine-tuned for 100 epochs with large force/stress loss ratios of 1, followed by further fine-tuning with force/stress loss ratios of 0.1. The learning rate is set to 1×10^{-3}. The resulting model is then employed for further calculations.

Finally, CSP under 50, 100, and 150 GPa is performed with the MAGUS code driven by the fine-tuned MatterSim model. For each pressure, more than 10 000 configurations are sampled and relaxed. In order to determine the stable phases in a wider pressure range, low-enthalpy structures found are relaxed at more pressures between 50 and 200 GPa. Moreover, to incorporate anharmonicity, the 100 lowest-enthalpy structures at 100 GPa are selected and relaxed using SSCHA and the obtained fine-tuned potential at 0 K and a wide range of pressures.

2. PdH

We extend the same methodology to PdH to further validate the robustness of our approach. Two independent iterative learning searches are performed at 0 and 50 GPa starting from the same MatterSim-v1.0.0-1M foundation model. The number of atoms ranges from 2 to 8. Each search comprises 10 generations with 100 structures per generation. After structural relaxations, 10 structures are randomly sampled from each generation and subjected to two distinct distortions. The distortion and fine-tuning procedures are kept identical to those described above.

The final training, validation, and test datasets from the two pressure searches contain 320, 40, and 40 configurations, respectively. The model is first fine-tuned for 300 epochs with force/stress loss ratios of 1, followed by further fine-tuning with force/stress loss ratios of 0.01. The learning rate is set to 1×10^{-4}. The resulting model is then employed for SSCHA calculations.

B. Settings of the SSCHA calculations

For H_3S, the SSCHA is used for evaluating thermodynamic stability and relaxing the crystal structures considering ionic quantum fluctuations and anharmonicity of various H_3S phases obtained by CSP. The SSCHA is also used to compute the free-energy Hessian matrices, which determine whether a structure is dynamically stable within the anharmonic free energy landscape [53], of cubic H_3S both with the obtained MLIP through the procedure described in Sec. III and DFT. In the former task, variable-cell SSCHA relaxations were performed on $2 \times 2 \times 2$ supercells at 100 GPa for all the structures. The significant acceleration of the MLIP compared to DFT allows us to perform SSCHA calculations efficiently, even for structures that because of their low symmetry require a large number of configurations. We adopt a high-throughput approach for the SSCHA calculations by generating 200 random configurations in each SSCHA population and limiting the SSCHA relaxation to a total of 50 populations, which guarantees a converged result. For free energy Hessian

calculations of cubic $Im\bar{3}m$ H_3S, variable-cell SSCHA relaxations were first performed on $3 \times 3 \times 3$ supercells from 50 to 250 GPa with the MLIP. We also adopt a high-throughput approach here by making use of 1000 random configurations at each population and running a total of 20 populations. DFT-driven SSCHA relaxations were performed more carefully to save computational time. The SSCHA relaxations started from the auxiliary dynamical matrix computed by the MLIP with fixed cell parameters and $2 \times 2 \times 2$ supercells. The number of configurations is set to 100 or 200 per population, which are enough to converge the results for this high-symmetry phase. Most DFT-SSCHA relaxations converged after 2 or 3 populations. Free-energy Hessian matrices and phonon frequencies [53] were then obtained *a posteriori* for both MLIP and DFT.

For PdH, the SSCHA calculations specifically focus on the rock-salt (RS) and zincblende (ZB) phases to evaluate their thermodynamic stability and vibrational properties. Variable-cell SSCHA relaxations are performed using the fine-tuned MLIP on $4 \times 4 \times 4$ supercells across a pressure range of 0 to 50 GPa at 0 K. For each SSCHA population, 100 random configurations are generated. These relaxations are followed by free-energy Hessian calculations using 500 configurations to determine the dynamical stability of the RS phase with anharmonicity. To validate, DFT-driven fixed-cell SSCHA relaxations are also performed on $2 \times 2 \times 2$ supercells. These calculations are initialized using the auxiliary dynamical matrices obtained from the MLIP with 100 configurations per population. Subsequently, DFT-driven free-energy Hessian matrices and anharmonic phonon frequencies are calculated to provide a direct comparison with the MLIP results.

C. DFT settings

For H_3S, the Perdew-Burke-Ernzerhof (PBE) functional [57] associated with pseudopotentials for H ($1s^2$) and S ($3s^2 3p^4$) implemented in the VASP [58–60] code is used for DFT calculations. A plane-wave cutoff energy of 500 eV and a Brillouin zone integration grid spacing of $2\pi \times 0.03$ Å^{-1} were used. Such settings are not of very high accuracy, but they are practical and comparable with settings used for crystal structure searching of H_3S in previous works [7,51].

For PdH, the PBE functional is also employed, with pseudopotentials for H ($1s^2$) and Pd ($4d^9 5s^1$). To ensure computational efficiency, a softer pseudopotential is chosen for H compared to the H_3S case, allowing for a lower plane-wave cutoff energy of 300 eV. The Brillouin zone integration grid spacing is $2\pi \times 0.05$ Å^{-1}. Similar to the H_3S settings, these parameters are chosen to balance practical performance with sufficient accuracy for the iterative learning and CSP of the PdH system.

D. Settings of the elastic calculations

Elastic constants of H_3S phases are computed using the stress-strain method with both PBE and the fine-tuned MatterSim potential via MatCalc [61]. The resulting moduli are used to verify that the MLIP can predict the mechanical properties accurately, without performing a detailed analysis of elastic properties in this work.

TABLE I. Root-mean-square errors of foundation and fine-tuned MatterSim models for H_3S. Fine-tuned values are shown in bold.

Dataset	Energy (meV/atom)	Force (meV/Å)	Stress (GPa)
Training	85.2/**6.1**	398.1/**117.7**	7.02/**0.48**
Validation	78.8/**6.6**	388.0/**142.4**	7.14/**1.14**
Test	85.3/**6.7**	409.0/**136.0**	6.88/**1.13**

V. RESULTS AND DISCUSSION

To evaluate the accuracy of the fine-tuned MatterSim potential to perform crystal structure predictions considering lattice anharmonicity as well as to estimate anharmonic vibrational frequencies, we use the well-studied H_3S system as a representative test case. According to enthalpy calculations in previous studies [7,30,51], the PBE functional predicts the following stability sequence for H_3S: $P1 \rightarrow C2/c$ (2 GPa) $\rightarrow$ $R3m$ (112 GPa) $\rightarrow$ $Im\bar{3}m$ (175–180 GPa). The $Im\bar{3}m$ phase was experimentally identified as a high-temperature superconductor at around 150 GPa [13] but it presents imaginary modes below 173 GPa [62], indicating that the structure is not a local minimum of the BO PES; in other words, the structure is dynamically unstable in HA at the pressures where the highest superconducting critical temperature was observed. This discrepancy is resolved by SSCHA calculations that account for anharmonicity, revealing that the $Im\bar{3}m$ phase becomes dynamically stable above approximately 100 GPa [30,62], much lower than the transition pressure predicted by static lattice calculations. Because H_3S is a challenging system for first-principles phonon calculations, it serves as an ideal benchmark for testing MatterSim's accuracy in predicting vibrational properties and phase stability under high pressure at the anharmonic level.

Apart from H_3S, we further examine PdH as another representative anharmonic system [33,35,63–65]. PdH has a face-centered cubic Pd sublattice with hydrogen atoms occupying interstitial sites. Static DFT calculations [63–65] suggest that the tetrahedral site (ZB-type) is energetically favorable at ambient pressure, whereas neutron diffraction experiments [66] identified hydrogen at octahedral sites (RS-type). Previous SSCHA calculations based on DFT [33,35] showed that anharmonic effects stabilize the octahedral sites and remove imaginary phonon modes, resolving the discrepancy between harmonic calculations and experiments. Because of its strong anharmonic effect, PdH provides a suitable test case to assess the accuracy of the fine-tuned potential in predicting phase stability and vibrational properties.

A. H_3S

1. Test on the foundation model

The MatterSim foundation model enables robust relaxations from random initial structures, but fails to predict stable phases under high pressures. As shown in Table I, the model exhibits energy root-mean-square errors (RMSEs) of approximately 80 meV/atom across training, validation, and test datasets. Such accuracy is too low for reliable stability determination, given that the energy difference between competing structures is of that order of magnitude [7]. For instance, as

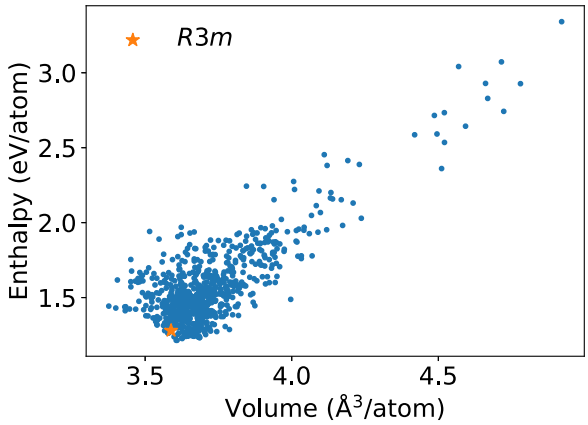

FIG. 2. The enthalpy–volume plots for H_3S phases predicted by the pretrained MatterSim foundation model at 150 GPa.

shown in Fig. 2, the ground state $R3m$ phase predicted by DFT is 65 meV/atom above the lowest enthalpy crystal structure obtained by the foundation MatterSim model at 150 GPa, and in the stability ranking it appears only at 60th place. This clearly highlights that foundation models by themselves are not enough for accurate thermodynamic stability calculations without further iterative training and fine-tuning.

2. Results obtained with the fine-tuned model

The fine-tuning procedure sketched above significantly enhances the accuracy of the MatterSim potential for the H_3S system, reducing energy RMSEs to only ∼6 meV/atom, thus allowing to identify stable phases correctly and yielding an error that is considerably lower than the impact of the ionic quantum fluctuations and anharmonicity on the total energy of the system [30]. Energy, force, and stress comparisons between the fine-tuned MatterSim model and reference DFT calculations are presented in Table I and Fig. 3. While force RMSEs are larger than 100 meV/Å, this performance remains acceptable considering the high diversity of the datasets, including molecular systems, metals, insulators, and various bonding patterns.

3. Vibrational properties

Once the accuracy of the fine-tuned potential has been verified, we move forward and perform SSCHA calculations for the high-symmetry $Im\bar{3}m$ phase of H_3S to estimate its phonon frequencies as obtained from the anharmonic free energy Hessian [62]. In this system, the soft optical mode T_{1u} at Γ within HA is related to the transition towards the $R3m$ phase. The squared frequencies of this mode as a function of pressure are computed using both the HA and the SSCHA. As shown in Fig. 4(a), the fine-tuned MatterSim predicts the critical pressure, where the frequency becomes zero, at the harmonic level in reasonable agreement with PBE-based calculations. However, there are still discrepancies in the frequencies between PBE and MatterSim at higher pressures, with the MLIP tending to underestimate frequency.

When the SSCHA is applied, the fine-tuned MatterSim and PBE results agree well across a broad pressure range. Although the training dataset was generated mainly at lower pressures [around 75 GPa and 125 GPa, indicated by dashed vertical lines in Fig. 4(a)], the fine-tuned potential accurately reproduces the anharmonic phonon frequencies over a much wider range, from 50 GPa to 240 GPa. The difference between the critical pressures predicted by PBE and the

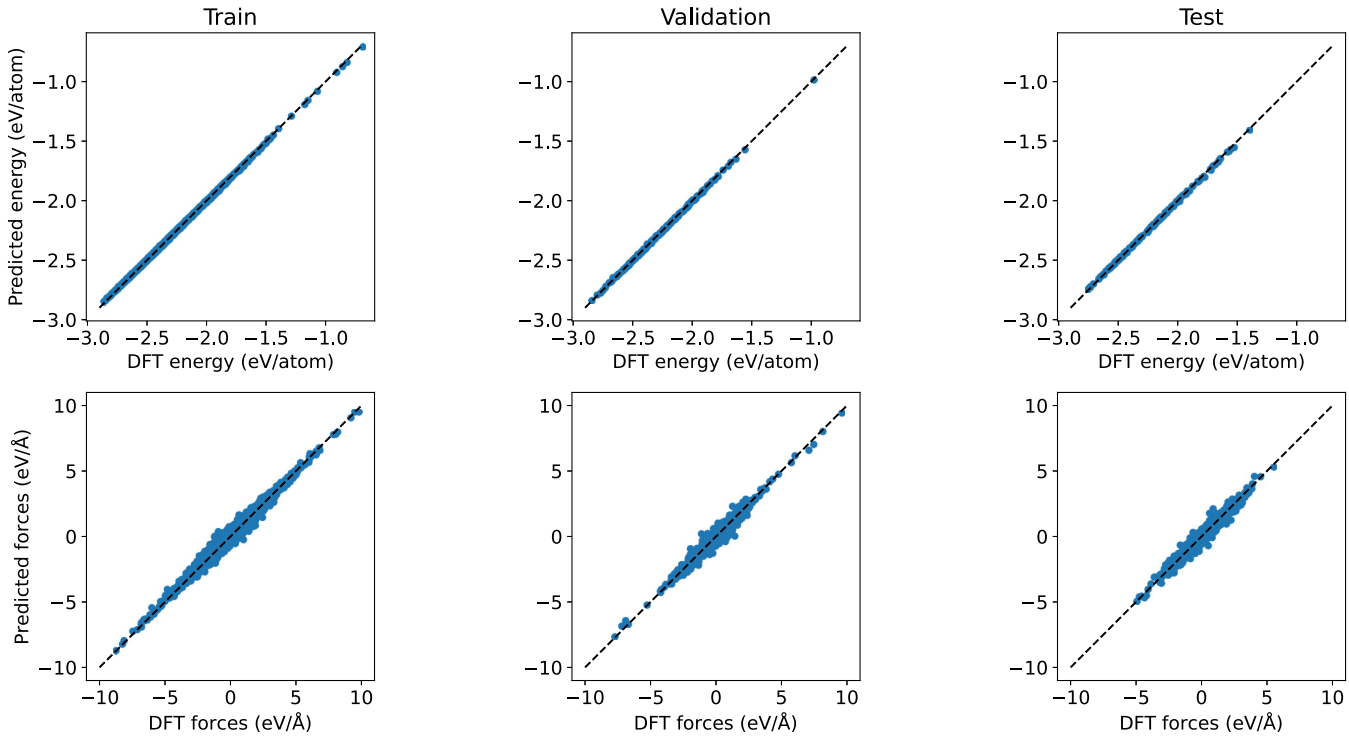

FIG. 3. Parity plots of energy (upper) and forces (lower) comparing fine-tuned MatterSim predictions and DFT reference data for H_3S.

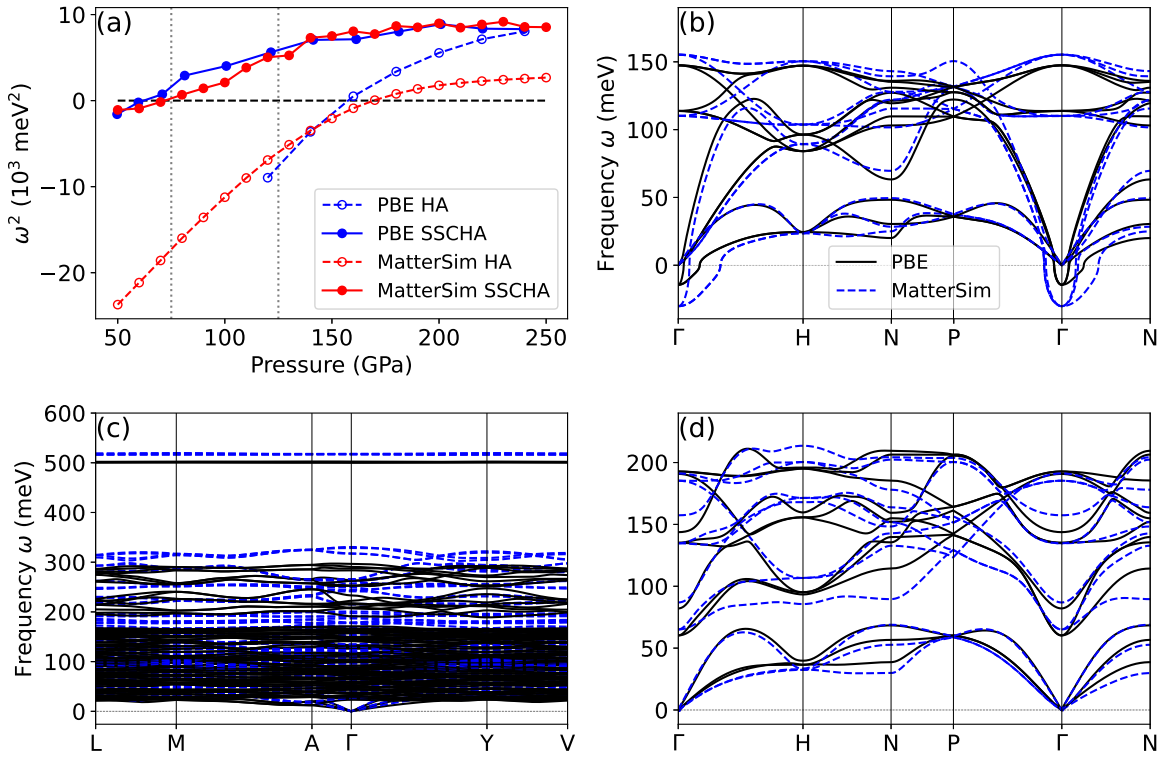

FIG. 4. (a) Squared frequency of the T_{1u} mode at Γ point of $Im\bar{3}m$ H_3S, as a function of the pressure, predicted by the fine-tuned MatterSim and PBE with HA and SSCHA. The gray dashed lines represent pressures for generating datasets. (b) Anharmonic phonon dispersions at 0 K from free-energy Hessian matrices for $Im\bar{3}m$ phase computed by PBE and the fine-tuned MatterSim under 60 GPa. The imaginary mode at Γ is the T_{1u} mode. (c) Harmonic phonon dispersions for $C2/c$ H_3S computed by PBE and the fine-tuned MatterSim under 120 GPa. (d) Harmonic phonon dispersions for $R3m$ H_3S computed by PBE and the fine-tuned MatterSim under 150 GPa.

fine-tuned MatterSim is within 10 GPa. Furthermore, as shown in Fig. 4(b), the potential can reproduce the major features of renormalized phonon dispersions computed by PBE for this highly anharmonic system around the critical pressure.

In addition to the $Im\bar{3}m$ phase, we also evaluate the performance of the fine-tuned MatterSim for the $R3m$ and $C2/c$ phases at HA level. As shown in Figs. 4(c) and 4(d), the phonon dispersions predicted by the fine-tuned potential are in agreement with the PBE results, especially for the $R3m$ phase. While the accuracy for the $C2/c$ phase is relatively lower, it is important to note that this phase is not in the training set. The accurate reproduction of its phonon spectrum therefore indicates the extrapolation capability of the fine-tuned MatterSim potential.

These results suggest that the fine-tuned MatterSim potential is reliable for both harmonic and anharmonic lattice dynamics calculations across multiple competing phases. Interestingly, the discrepancy between the fine-tuned MatterSim and PBE is smaller within the SSCHA framework than within the HA. We note that this behavior is not expected to be specific to MatterSim, and similar trends could occur for other foundation models in a comparable workflow.

4. Phase diagram with and without anharmonicity

Next, we evaluate the accuracy of the obtained MLIP in phase diagram calculations with and without anharmonic effects. As shown in Fig. 5, the $C2/c$ phase is most stable below 100 GPa when the enthalpy is calculated from the BO PES without considering lattice anharmonicity [51]. This result is consistent with the transition pressure of 112 GPa predicted by PBE [51], indicating the predictive accuracy of the MLIP for relative phase stability over a broad pressure range, even for phases not included in the training dataset.

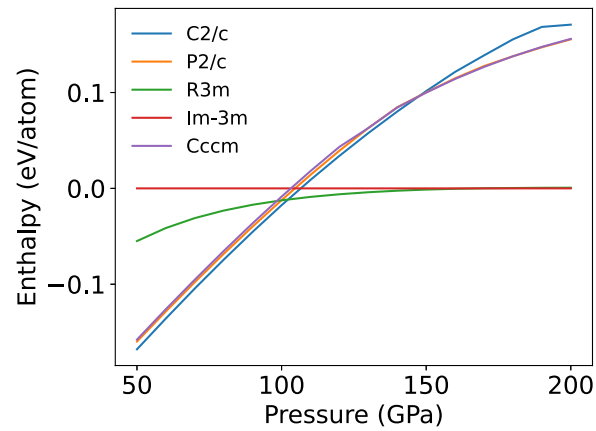

FIG. 5. Relative enthalpy at the classical BO level without considering anharmonic effects of H_3S phases, as a function of the pressure, predicted by the fine-tuned MatterSim. The $Im\bar{3}m$ phase is set as the reference system.

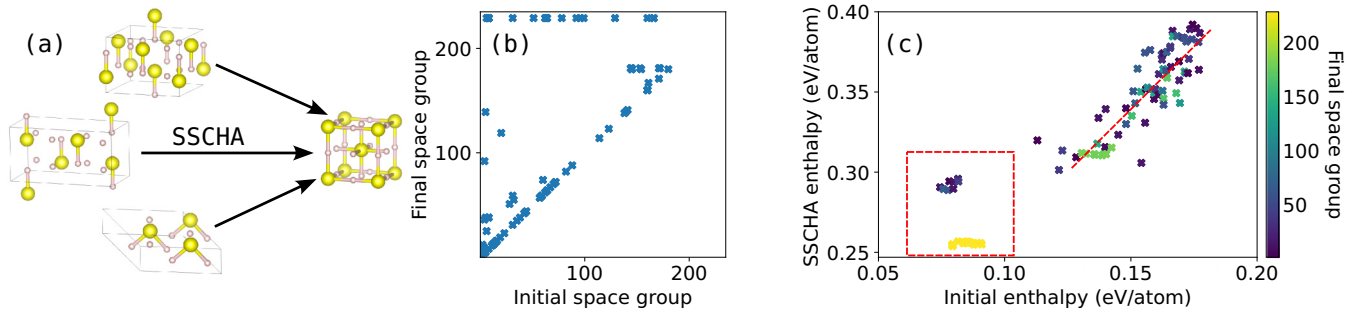

FIG. 6. (a) Structural transformations from metastable H_3S phases to the cubic phase by SSCHA relaxations. (b) Symmetry analysis and (c) thermodynamic stability of H_3S phases before and after SSCHA relaxations at 100 GPa. In (c), the final space group of each relaxed structure is indicated by a colormap, with color corresponding to space group number. The red dashed box highlights a reordering of stability ranking in low-enthalpy region, while the red line indicates nearly linear correlation in high-enthalpy region.

To incorporate anharmonicity into the phase diagram, we first perform CSP at 100 GPa with the fine-tuned MatterSim. Then, we extract the 100 distinct structures with the lowest enthalpies and perform fully variable-cell SSCHA relaxations at 0 K. This task is computationally prohibitive for DFT-based SSCHA and clearly benefits from the speed of MLIPs. As shown in Figs. 6(a) and 6(b), 18 of these configurations transform into the high-symmetry $Im\bar{3}m$ phase after the SSCHA relaxation. To make sure that this phenomenon is not an artifact of the MLIP, we performed PBE-driven relaxations for these configurations. Most of them retained their original space group symmetry after subsequent PBE relaxations, demonstrating the reliability of the fine-tuned MatterSim model in predicting metastable phase configurations. Figure 6(c) confirms the cubic H_3S phase as the global minimum after SSCHA relaxations, extending previous findings on stabilization induced by quantum fluctuations [30,32] across a significantly broader free energy surface. Notably, Fig. 6(c) also reveals that while SSCHA introduces corrections of around 200 meV/atom with respect to initial enthalpies, it significantly affects the stability ranking of configurations with low formation enthalpies (below 50 meV/atom, indicated by a red box). Beyond this region, the initial and SSCHA enthalpies exhibit a nearly linear correlation, highlighted by a red line in Fig. 6(c). This indicates that performing SSCHA on the set of low-energy configurations is sufficient to capture the major stable phases, without the need to treat all high-enthalpy structures, thus simplifying CSP with thermal and quantum fluctuations. Extended analysis at 300 K and 600 K shows that thermal effects have a minor impact on H_3S phase stability (see Fig. 7). This confirms that nuclear quantum effects are the primary factor determining the relative stability of H_3S phases.

5. Elastic properties

To further assess the capabilities of the fine-tuned MatterSim potential, we computed the elastic constants of various H_3S phases at different pressures, as shown in Table II. The predicted elastic moduli are in good agreement with reference DFT calculations, demonstrating that the potential not only reproduces energies, forces, and phonons, but also captures the mechanical response of the crystal. Although a detailed discussion of elastic properties is beyond the scope of this work, this result confirms the versatility of the fine-tuned MatterSim potential.

B. PdH

Energy, force, and stress RMSEs of the fine-tuned MatterSim model for PdH are summarized in Table III. The fine-tuning procedure significantly improves the accuracy of the MatterSim potential for the PdH system. Compared to H_3S, the force RMSEs are lower, even for the pretrained MatterSim. This difference can be attributed to the lower pressure range to generate PdH datasets, the smaller number of atoms per unit cell, and the relatively simple bonding environment. The achieved accuracy enables a reliable description of relative phase stability.

As shown in Fig. 8(a), ZB-PdH has a lower energy than RS-PdH by 47 meV/atom at 0 GPa on the BO-PES computed by PBE. This value is consistent with previous high-precision PBE calculations [64], which reported an energy difference of 83 meV per formula unit (41.5 meV/atom). For the fine-tuned MatterSim, the corresponding BO energy difference is 40 meV/atom, in good agreement with DFT results. For phonon within HA, there is an imaginary optical mode at Γ at 0 GPa,

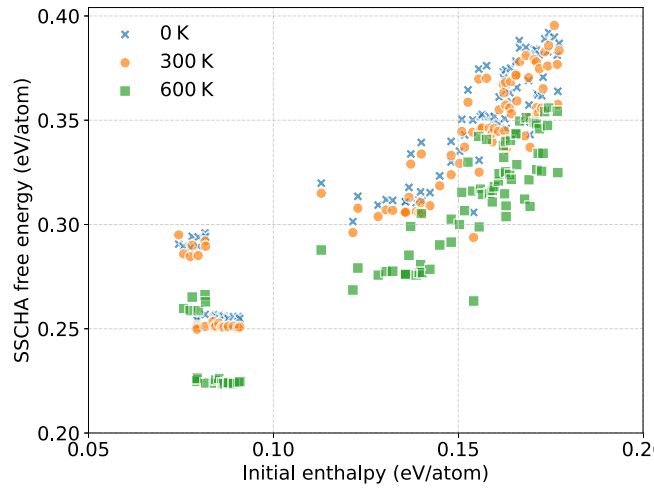

FIG. 7. Thermodynamic stability of H_3S phases at 100 GPa and temperatures of 0, 300, and 600 K, comparing initial enthalpies with SSCHA free energies.

TABLE II. Bulk modulus (K) and shear modulus (G) of H_3S phases predicted by PBE and fine-tuned MatterSim models.

	$I\bar{m}3m$ at 200 GPa		$R3m$ at 150 GPa		$C2/c$ at 120 GPa	
	K (GPa)	G (GPa)	K (GPa)	G (GPa)	K (GPa)	G (GPa)
PBE	709	264	569	226	469	265
MatterSim	708	290	563	249	456	240

consistent with previous DFT calculations [33], as shown in Fig. 8(b). This indicates that the RS phase is dynamically unstable. As the pressure increases, RS-PdH becomes energetically more stable and the imaginary mode also vanishes within HA around 10 GPa.

When anharmonic effects are included within the SSCHA, the relative stability is reversed. At 0 GPa and 0 K, the SSCHA energy of ZB-PdH becomes higher than that of RS-PdH by 17.6 and 8.9 meV/atom, as computed by PBE and the fine-tuned MatterSim, respectively. This change indicates a large anharmonic correction more than 60 meV/atom. Since the energy error of the fine-tuned MatterSim is much smaller than this anharmonic contribution, the potential is able to correctly capture the stabilization of the RS phase driven by anharmonic effects, in agreement with experiments and previous DFT calculations [35].

The phonon frequencies obtained from the free-energy Hessian further confirm the dynamical stability of the RS phase, as shown in Fig. 8(b). Similar to the H_3S case, the fine-tuned MatterSim potential shows higher accuracy in SSCHA calculations than in standard harmonic phonon calculations. For example, at 0 GPa the difference in the squared frequency is 1.42×10^3 meV^2 within the HA, while it is reduced to 0.85×10^3 meV^2 within the SSCHA.

Compared to H_3S, the improvement from the SSCHA is less pronounced for PdH, especially at high pressures. Several factors may contribute to this behavior. First, the force RMSEs of PdH are much lower than those of H_3S, so harmonic phonon frequencies are already predicted with relatively high accuracy. Second, as discussed in Sec. III A, the iterative learning strategy tends to sample more low-energy configurations. The PdH datasets were generated from structure searches at 0 and 50 GPa. At 0 GPa, RS-PdH is not energetically favorable, so this phase is sampled less frequently. In contrast, RS-PdH is the most stable phase at 50 GPa and is therefore well sampled, leading to very good agreement in harmonic phonon frequencies at high pressures around 50 GPa. Thus, SSCHA combined with the fine-tuned MLIP still yields a systematic improvement over the harmonic approximation, especially when the MLIP accuracy is limited, indicating that this improvement is not system-specific.

TABLE III. Root-mean-square errors of foundation and fine-tuned MatterSim models for PdH. Fine-tuned values are shown in bold.

Dataset	Energy (meV/atom)	Force (meV/Å)	Stress (GPa)
Training	51.3/**3.4**	91.7/**52.8**	4.04/**1.04**
Validation	57.0/**6.0**	79.3/**44.7**	3.83/**1.13**
Test	49.1/**4.9**	68.4/**47.8**	4.09/**1.01**

C. Improved accuracy of the SSCHA calculations with the MLIP

As clearly shown above, the results for the vibrational properties obtained with the fine-tuned MLIP are closer to the DFT results at the SSCHA level than at the harmonic level. Also, the crystal structure search performed at the SSCHA level with the fine-tuned MatterSim potential is consistent with previous DFT + SSCHA results [30]. All these observations suggest that, because of a certain cancellation of errors, SSCHA calculations tolerate moderate MLIP errors better than the standard BO PES calculations at the level of the harmonic approximation, for both dynamical and thermodynamic properties.

In order to deepen this idea, we first note that, as discussed in Sec. II, the performance of MLIP for SSCHA depends on its accuracy to evaluate the gradients of the SSCHA free energy. To compare the accuracy of the MLIP in SSCHA relaxation with that in a standard BO relaxation, we show below how the key quantities are computed.

Given centroids $\boldsymbol{\mathcal{R}} = \tilde{\boldsymbol{R}}$ and an auxiliary force constant matrix $\boldsymbol{\Phi}$, we generate an ensemble of configurations by sampling the associated SSCHA density matrix. For each configuration i, the BO forces $\mathbf{f}^{\mathrm{MLIP}}(\boldsymbol{R}_i)$ and $\mathbf{f}^{\mathrm{DFT}}(\boldsymbol{R}_i)$ are computed using DFT and the fine-tuned MLIP, respectively. The individual force errors are

$$\Delta\mathbf{f}^{\mathrm{BO}}(\boldsymbol{R}_i) = \mathbf{f}^{\mathrm{MLIP}}(\boldsymbol{R}_i) - \mathbf{f}^{\mathrm{DFT}}(\boldsymbol{R}_i), \tag{11}$$

and the full distribution of errors is obtained by collecting all components of $\Delta\mathbf{f}^{\mathrm{BO}}(\boldsymbol{R}_i)$ across the ensemble. The RMSE of the forces is then given by

$$\mathrm{RMSE}_f = \sqrt{\frac{1}{N}\sum_{i,a}\left|\Delta f_a^{\mathrm{BO}}(\mathbf{R}_i)\right|^2}, \tag{12}$$

where a labels atomic force components and N is the total number of components.

From the same ensemble, we can also compute the SSCHA free-energy gradients $\frac{\partial\mathcal{F}}{\partial\boldsymbol{\mathcal{R}}}|_{\boldsymbol{\mathcal{R}}=\tilde{\boldsymbol{R}}}$ for the configuration $\tilde{\boldsymbol{R}}$ using both DFT and MLIP [Eq. (8)]. The error in the free-energy gradient is defined as

$$\Delta\left(\left.\frac{\partial\mathcal{F}}{\partial\boldsymbol{\mathcal{R}}}\right|_{\boldsymbol{\mathcal{R}}=\tilde{\boldsymbol{R}}}\right) = \left.\frac{\partial\mathcal{F}^{\mathrm{MLIP}}}{\partial\boldsymbol{\mathcal{R}}}\right|_{\boldsymbol{\mathcal{R}}=\tilde{\boldsymbol{R}}} - \left.\frac{\partial\mathcal{F}^{\mathrm{DFT}}}{\partial\boldsymbol{\mathcal{R}}}\right|_{\boldsymbol{\mathcal{R}}=\tilde{\boldsymbol{R}}}. \tag{13}$$

We also compute the BO forces $\frac{\partial V}{\partial\boldsymbol{R}}$ at the centroid positions $\tilde{\boldsymbol{R}}$ to compare the accuracy of MLIP for standard BO-based relaxation with that for SSCHA-based relaxation,

$$\Delta\left(\left.\frac{\partial V}{\partial\boldsymbol{R}}\right|_{\boldsymbol{R}=\tilde{\boldsymbol{R}}}\right) = \left.\frac{\partial V^{\mathrm{MLIP}}}{\partial\boldsymbol{R}}\right|_{\boldsymbol{R}=\tilde{\boldsymbol{R}}} - \left.\frac{\partial V^{\mathrm{DFT}}}{\partial\boldsymbol{R}}\right|_{\boldsymbol{R}=\tilde{\boldsymbol{R}}}. \tag{14}$$

Their distributions and RMSEs are evaluated in the same way as for the forces.

For the free-energy gradients with respect to the auxiliary force-constant matrix $\boldsymbol{\Phi}$, we calculate the per-configuration quantities and the averaged gradient

$$\begin{aligned}\Delta\mathcal{G}_i^{\boldsymbol{\Phi}} &= \mathcal{G}_i^{\boldsymbol{\Phi},\mathrm{MLIP}} - \mathcal{G}_i^{\boldsymbol{\Phi},\mathrm{DFT}},\\ \Delta\mathcal{G}^{\boldsymbol{\Phi}} &= \mathcal{G}^{\boldsymbol{\Phi},\mathrm{MLIP}} - \mathcal{G}^{\boldsymbol{\Phi},\mathrm{DFT}},\end{aligned} \tag{15}$$

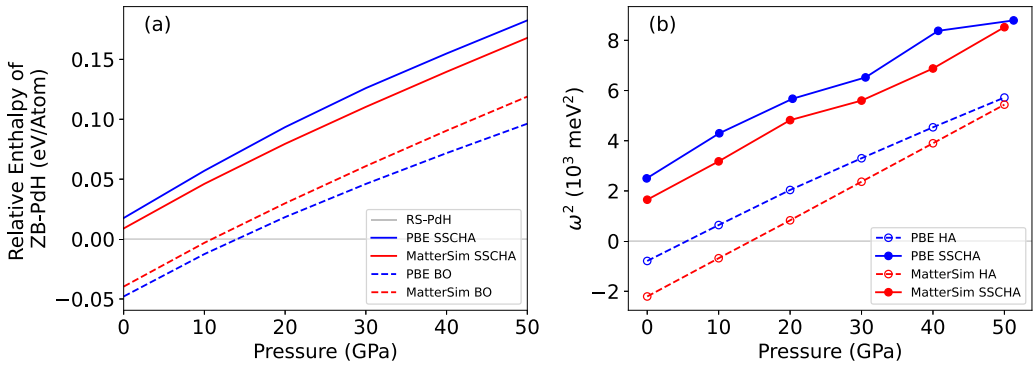

FIG. 8. (a) Relative enthalpy of the ZB phase of PdH with respect to the RS phase. For both PBE and the fine-tuned MatterSim potential, the enthalpy is evaluated at the BO level and within the SSCHA. (b) Squared frequency of the soft mode at Γ point of PdH RS phase, as a function of the pressure, predicted by the fine-tuned MatterSim and PBE with HA and SSCHA at 0 K.

as defined in Eqs. (9) and 10 using forces computed by MLIP and DFT. Their error distributions and RMSEs are computed in the same way.

Based on the procedure described above, we can now evaluate how ensemble averaging affects the apparent accuracy of the MLIP. We first consider cubic $I\bar{m}3m$ H_3S at 60 GPa and 0 K. An ensemble of 500 configurations is generated using the converged auxiliary dynamical matrix from the SSCHA relaxation performed with PBE. Then, the forces of these configurations $\{\mathbf{f}^{\mathrm{BO}}(\boldsymbol{R}_i)\}$ are computed using both the fine-tuned MatterSim model and PBE. For this ensemble, the RMSE of the atomic forces [Eq. (12)] is 129 meV/Å [Fig. 9(a)], consistent with those in Table I. However, when the same ensemble is used to evaluate the SSCHA free-energy gradient $\frac{\partial \mathcal{F}}{\partial \boldsymbol{\mathcal{R}}}$, the RMSE decreases drastically to only 4.5 meV/Å [Fig. 9(b)]. This large reduction comes from the nearly symmetric distribution of individual force errors [Fig. 9(a)], where over- and underestimations effectively cancel upon ensemble averaging. A similar compensation also occurs for free-energy gradients with respect to the auxiliary force-constant matrix $\mathcal{G}^{\boldsymbol{\Phi}}_{ab}$, where averaged gradients show smaller errors compared to the individual contributions $\{\mathcal{G}^{\boldsymbol{\Phi}}_{i,ab}\}$ [Figs. 9(c) and 9(d)].

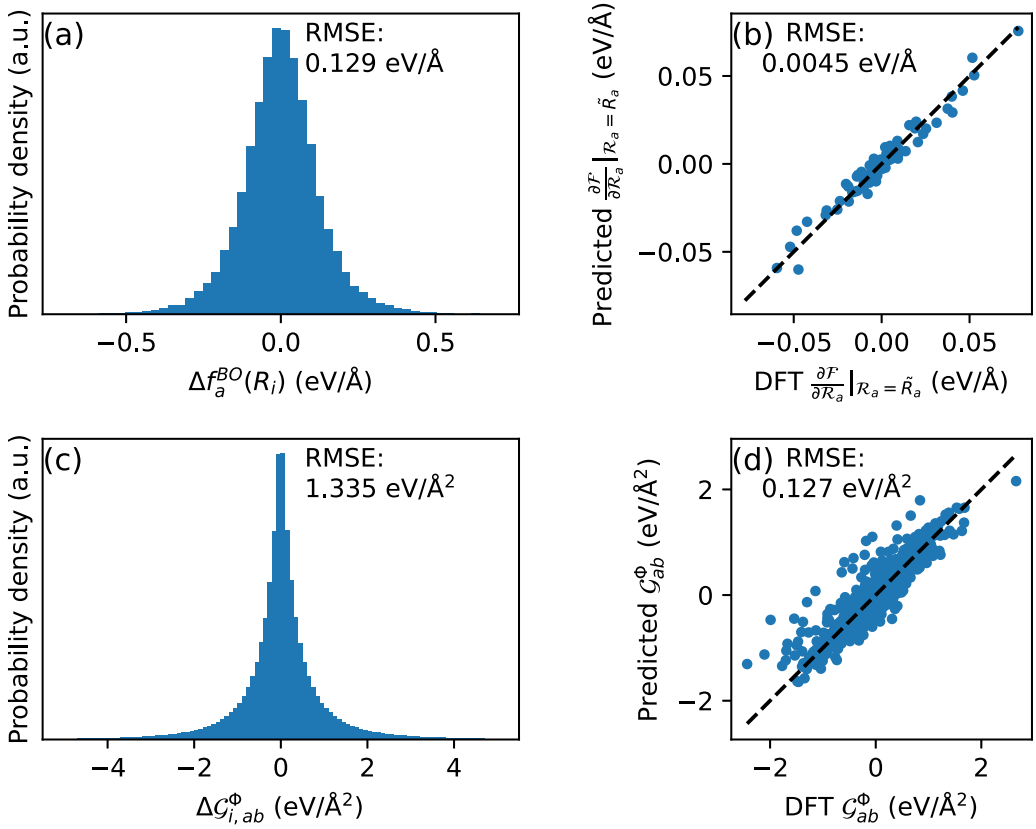

FIG. 9. Distributions of gradient errors and parity plots comparing fine-tuned MatterSim predictions with DFT reference data for the $I\bar{m}3m$ phase of H_3S. (a) Distribution of $\{\Delta\mathbf{f}^{\mathrm{BO}}(\boldsymbol{R}_i)\}$. (b) Parity plot for $\frac{\partial \mathcal{F}}{\partial \boldsymbol{\mathcal{R}}}|_{\boldsymbol{\mathcal{R}}=\tilde{\boldsymbol{R}}}$. (c) Distribution of $\{\Delta\boldsymbol{\mathcal{G}}^{\boldsymbol{\Phi}}_i\}$. (d) Parity plot for $\boldsymbol{\mathcal{G}}^{\boldsymbol{\Phi}}$.

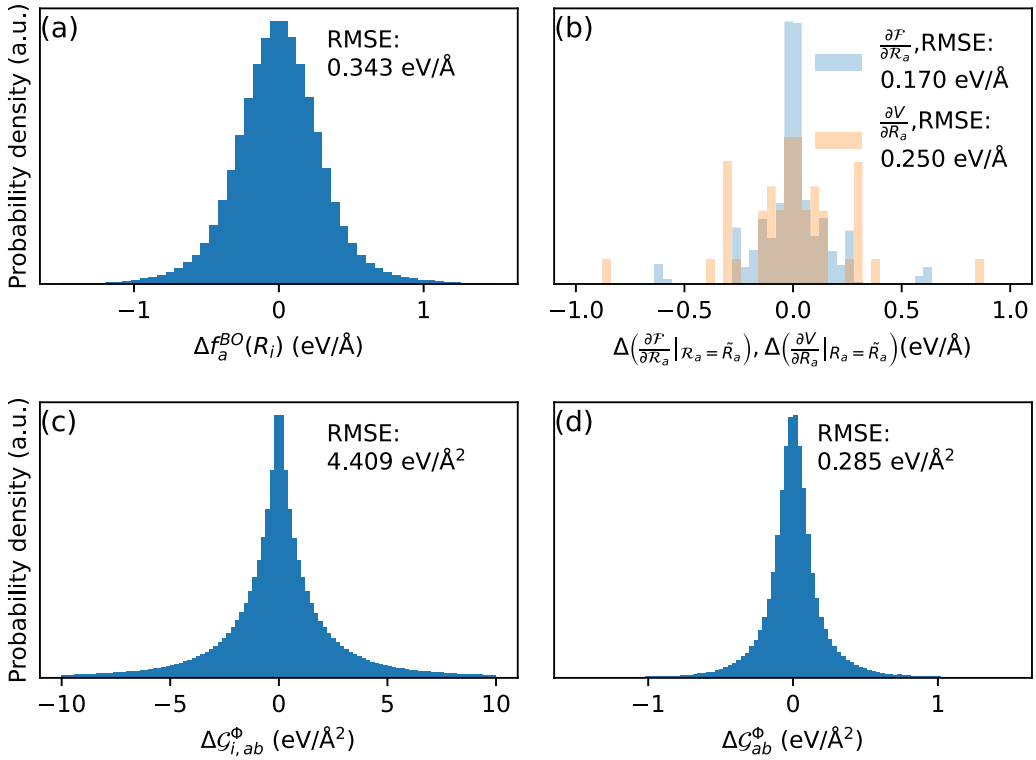

FIG. 10. Distributions of gradient errors in the $C2/c$ phase of H_3S: (a) $\{\Delta\mathbf{f}^{\mathrm{BO}}(\boldsymbol{R}_i)\}$, (b) $\Delta(\frac{\partial \mathcal{F}}{\partial \boldsymbol{\mathcal{R}}}|_{\boldsymbol{\mathcal{R}}=\tilde{\boldsymbol{R}}})$ and $\Delta(\frac{\partial V}{\partial \boldsymbol{R}}|_{\boldsymbol{R}=\tilde{\boldsymbol{R}}})$, (c) $\{\Delta\boldsymbol{\mathcal{G}}^{\boldsymbol{\Phi}}_i\}$, (d) $\Delta\boldsymbol{\mathcal{G}}^{\boldsymbol{\Phi}}$.

Because of the high symmetry of the $Im\bar{3}m$ phase, the gradients with respect to the centroids ideally vanish in practical SSCHA relaxations. The small residual values observed in Fig. 9(b) arise from finite sampling and the removal of symmetry constraints during averaging. To further assess the averaging effect in a lower-symmetry system, we performed the same analysis for the monoclinic $C2/c$ phase of H_3S at 100 GPa. Similar to the $Im\bar{3}m$ case, 500 configurations were generated, but here the auxiliary force-constant matrix and the configuration were optimized by SSCHA driven by the fine-tuned MatterSim model instead of PBE. Since the $C2/c$ phase was not included in the training data, the RMSE of $\mathbf{f}_{\mathrm{BO}}(\boldsymbol{R}_i)$ is larger, reaching 343 meV/Å [Fig. 10(a)]. The ensemble-averaged gradient $\frac{\partial \mathcal{F}}{\partial \boldsymbol{\mathcal{R}}}$, however, shows a reduced error of 170 meV/Å, corresponding to a 50% decrease [Fig. 10(b)]. Although this reduction is smaller than in the high-symmetry phase, a clear improvement is still achieved compared with the individual forces.

The RMSE of BO forces at centroids $(\frac{\partial \mathcal{V}}{\partial \boldsymbol{R}}|_{\boldsymbol{R}=\tilde{\boldsymbol{R}}})$ is 250 meV/Å [Fig. 10(b)], which is higher than that of free-erngy gradient $\frac{\partial \mathcal{F}}{\partial \boldsymbol{\mathcal{R}}}|_{\boldsymbol{\mathcal{R}}=\tilde{\boldsymbol{R}}}$ for the same structure (170 meV/Å). This indicates that the MLIP reproduces free-energy gradients more accurately than potential-energy gradients, suggesting that SSCHA relaxations driven by MLIPs can be more reliable than standard relaxations. In some cases, MLIPs may even provide a more accurate description of the free-energy surface than the underlying BO-PES. Furthermore, although the errors in $\mathcal{G}^{\boldsymbol{\Phi}}_{ab}$ and $\{\mathcal{G}^{\boldsymbol{\Phi}}_{i,ab}\}$ are larger than those in the cubic phase, the relative error reduction is even more pronounced, as shown in Figs. 10(c) and 10(d). These results demonstrate that ensemble averaging in SSCHA provides robust error cancellation, even when the underlying MLIP force predictions are of limited accuracy.

VI. CONCLUSIONS

To enable CSP with anharmonic lattice dynamics, we proposed an iterative learning framework combining EA, an atomic foundation model, and SSCHA relaxations. MLIPs fine-tuned from foundation models significantly reduce the required training data while enabling efficient SSCHA calculations to account for anharmonic effects. We validate this approach by successfully reproducing phase stabilities of H_3S and PdH across a wide pressure range.

Two key insights emerge for CSP with anharmonicity. Firstly, although SSCHA requires more static calculations than HA and standard relaxations, highly accurate SSCHA frequencies and free energies can be obtained by using a moderate-accuracy MLIP. This advantage arises from error compensation during ensemble averaging. Overestimations and underestimations cancel, reducing net errors in ensemble-averaged properties. This compensation remains even when the MLIP force predictions are relatively poor. Secondly, free energy corrections caused by anharmonic and temperature effects do not change the stability ranking dramatically, even for highly anharmonic systems like H_3S and PdH. This insight suggests that SSCHA relaxations on a limited number of low-enthalpy configurations are sufficient, avoiding exhaustive SSCHA calculations for all the configurations, thus enabling practical CSP with anharmonic lattice dynamics.

The proposed approach in this work paves the way for practical CSP with anharmonicity. Future work will focus

on further reducing computational costs and enhancing the robustness of this approach for a broader range of materials.

ACKNOWLEDGMENTS

This project is funded by the Spanish Ministry of Science and Innovation (Grant No. PID2022142861NA-I00) and the Department of Education, Universities and Research of the Eusko Jaurlaritza and the University of the Basque Country UPV/EHU (Grant No. IT1527-22). The authors acknowledge financial support from the IKUR Strategy under the collaboration agreement between the Ikerbasque Foundation and the Centro de Física de Materiales (CFM-MPC) on behalf of the Department of Science, Universities and Innovation of the Basque Government (HPCAI21: AI-CrysPred). This project is also partially funded by the Extraordinary Grant of CSIC (Grant No. 2025ICT122). Y.-W.F. and I.E. acknowledge PRACE for awarding access to the EuroHPC supercomputer LUMI, located in CSC's data center in Kajaani, Finland, through the EuroHPC Joint Undertaking (EHPC-REG-2022R03-090 and EHPC-REG-2024R01-084). Technical and human support provided by DIPC Supercomputing Center is gratefully acknowledged. The authors acknowledge enlightening discussions with the partners of the SuperC collaboration. The authors thank Đorđe Dangić at UPV/EHU and Yu Han at Nanjing University for helpful discussions.

DATA AVAILABILITY

The data that support the findings of this article are openly available [67].

[1] L. Zhang, Y. Wang, J. Lv, and Y. Ma, Materials discovery at high pressures, Nat. Rev. Mater. **2**, 17005 (2017).

[2] A. R. Oganov, C. J. Pickard, Q. Zhu, and R. J. Needs, Structure prediction drives materials discovery, Nat. Rev. Mater. **4**, 331 (2019).

[3] P. Avery, X. Wang, C. Oses, E. Gossett, D. M. Proserpio, C. Toher, S. Curtarolo, and E. Zurek, Predicting superhard materials via a machine learning informed evolutionary structure search, npj Comput. Mater. **5**, 89 (2019).

[4] C.-N. Li, H.-P. Liang, B.-Q. Zhao, S.-H. Wei, and X. Zhang, Machine learning assisted crystal structure prediction made simple, J. Mater. Inf. **4**, 15 (2024).

[5] F. Peng, Y. Sun, C. J. Pickard, R. J. Needs, Q. Wu, and Y. Ma, Hydrogen clathrate structures in rare earth hydrides at high pressures: Possible route to room-temperature superconductivity, Phys. Rev. Lett. **119**, 107001 (2017).

[6] Y. Sun, J. Lv, Y. Xie, H. Liu, and Y. Ma, Route to a superconducting phase above room temperature in electron-doped hydride compounds under high pressure, Phys. Rev. Lett. **123**, 097001 (2019).

[7] D. Duan, Y. Liu, F. Tian, D. Li, X. Huang, Z. Zhao, H. Yu, B. Liu, W. Tian, and T. Cui, Pressure-induced metallization of dense $(H_2S)_2H_2$ with high-T_c superconductivity, Sci. Rep. **4**, 6968 (2014).

[8] H. Liu, I. I. Naumov, R. Hoffmann, N. W. Ashcroft, and R. J. Hemley, Potential high-T_c superconducting lanthanum and yttrium hydrides at high pressure, Proc. Natl. Acad. Sci. **114**, 6990 (2017).

[9] I. A. Kruglov, D. V. Semenok, H. Song, R. Szczęśniak, I. A. Wrona, R. Akashi, M. M. Davari Esfahani, D. Duan, T. Cui, A. G. Kvashnin, and A. R. Oganov, Superconductivity of LaH_{10} and LaH_{16} polyhydrides, Phys. Rev. B **101**, 024508 (2020).

[10] W. Cui, T. Bi, J. Shi, Y. Li, H. Liu, E. Zurek, and R. J. Hemley, Route to high-T_c superconductivity via Ch_4-intercalated H_3S hydride perovskites, Phys. Rev. B **101**, 134504 (2020).

[11] P. Liu, Q. Zhuang, Q. Xu, T. Cui, and Z. Liu, Mechanism of high-temperature superconductivity in compressed H_2-molecular–type hydride, Sci. Adv. **11**, eadt9411 (2025).

[12] S. Di Cataldo, C. Heil, W. von der Linden, and L. Boeri, $LaBh_8$: Towards high-T_c low-pressure superconductivity in ternary superhydrides, Phys. Rev. B **104**, L020511 (2021).

[13] A. P. Drozdov, M. I. Eremets, I. A. Troyan, V. Ksenofontov, and S. I. Shylin, Conventional superconductivity at 203 kelvin at high pressures in the sulfur hydride system, Nature (London) **525**, 73 (2015).

[14] A. P. Drozdov, P. P. Kong, V. S. Minkov, S. P. Besedin, M. A. Kuzovnikov, S. Mozaffari, L. Balicas, F. F. Balakirev, D. E. Graf, V. B. Prakapenka, *et al.*, Superconductivity at 250 K in lanthanum hydride under high pressures, Nature (London) **569**, 528 (2019).

[15] M. Somayazulu, M. Ahart, A. K. Mishra, Z. M. Geballe, M. Baldini, Y. Meng, V. V. Struzhkin, and R. J. Hemley, Evidence for superconductivity above 260 K in lanthanum superhydride at megabar pressures, Phys. Rev. Lett. **122**, 027001 (2019).

[16] I. Osmond, O. Moulding, S. Cross, T. Muramatsu, A. Brooks, O. Lord, T. Fedotenko, J. Buhot, and S. Friedemann, Clean-limit superconductivity in $Im\bar{3}m$ H_3S synthesized from sulfur and hydrogen donor ammonia borane, Phys. Rev. B **105**, L220502 (2022).

[17] Đ. Dangić, G. Caldarelli, R. Bianco, I. Savić, and I. Errea, Lattice thermal conductivity in the anharmonic overdamped regime, Phys. Rev. B **111**, 104314 (2025).

[18] J. M. Skelton, L. A. Burton, S. C. Parker, A. Walsh, C.-E. Kim, A. Soon, J. Buckeridge, A. A. Sokol, C. R. A. Catlow, A. Togo, and I. Tanaka, Anharmonicity in the high-temperature *Cmcm* Phase of SnSe: Soft modes and three-phonon interactions, Phys. Rev. Lett. **117**, 075502 (2016).

[19] Y. Lu, F.-w. Zheng, Y. Yang, P. Zhang, and D.-B. Zhang, Phase stabilities of *Cmcm* and *Pnma* SnSe studied by phonon quasiparticle approach, Phys. Rev. B **100**, 054304 (2019).

[20] R. Fei, W. Kang, and L. Yang, Ferroelectricity and phase transitions in monolayer group-IV monochalcogenides, Phys. Rev. Lett. **117**, 097601 (2016).

[21] A. Dewandre, O. Hellman, S. Bhattacharya, A. H. Romero, G. K. H. Madsen, and M. J. Verstraete, Two-step phase transition in SnSe and the origins of its high power factor from first principles, Phys. Rev. Lett. **117**, 276601 (2016).

[22] K. Wang, S. Chen, S.-W. Kim, and B. Monserrat, Origin of competing charge density waves in kagome metal ScV_6Sn_6, Nat. Commun. **15**, 10428 (2024).

[23] C. Verdi, L. Ranalli, C. Franchini, and G. Kresse, Quantum paraelectricity and structural phase transitions in strontium

titanate beyond density functional theory, Phys. Rev. Mater. **7**, L030801 (2023).

[24] F. Libbi, A. Johansson, B. Kozinsky, and L. Monacelli, Nonequilibrium quantum dynamics in $SrTiO_3$ under impulsive THz radiation with machine learning, Sci. Adv. **11**, eadw1634 (2025).

[25] Y.-W. Fang, H.-C. Ding, W.-Y. Tong, W.-J. Zhu, X. Shen, S.-J. Gong, X.-G. Wan, and C.-G. Duan, First-principles studies of multiferroic and magnetoelectric materials, Sci. Bull. **60**, 156 (2015).

[26] J. Diego, A. H. Said, S. K. Mahatha, R. Bianco, L. Monacelli, M. Calandra, F. Mauri, K. Rossnagel, I. Errea, and S. Blanco-Canosa, van der Waals driven anharmonic melting of the 3D charge density wave in VSe_2, Nat. Commun. **12**, 598 (2021).

[27] A. Girard, V. Ilakovac, M. Stekiel, W. Morgenroth, H. Berger, T. Yoshikazu, T. Hasegawa, A. Bosak, and B. Winkler, Soft-phonon driven hexagonal-orthorhombic phase transition in $BaVS_3$, Phys. Rev. B **99**, 144104 (2019).

[28] C.-S. Lian, C. Heil, X. Liu, C. Si, F. Giustino, and W. Duan, Coexistence of superconductivity with enhanced charge density wave order in the two-dimensional limit of $TaSe_2$, J. Phys. Chem. Lett. **10**, 4076 () (2019).

[29] C.-S. Lian, C. Si, and W. Duan, Unveiling charge-density wave, superconductivity, and their competitive nature in two-dimensional $NbSe_2$, Nano Lett. **18**, 2924 () (2018).

[30] I. Errea, M. Calandra, C. J. Pickard, J. R. Nelson, R. J. Needs, Y. Li, H. Liu, Y. Zhang, Y. Ma, and F. Mauri, Quantum hydrogen-bond symmetrization in the superconducting hydrogen sulfide system, Nature (London) **532**, 81 (2016).

[31] I. Errea, F. Belli, L. Monacelli, A. Sanna, T. Koretsune, T. Tadano, R. Bianco, M. Calandra, R. Arita, F. Mauri, and J. A. Flores-Livas, Quantum crystal structure in the 250-kelvin superconducting lanthanum hydride, Nature (London) **578**, 66 (2020).

[32] I. Errea, M. Calandra, C. J. Pickard, J. Nelson, R. J. Needs, Y. Li, H. Liu, Y. Zhang, Y. Ma, and F. Mauri, High-pressure hydrogen sulfide from first principles: A strongly anharmonic phonon-mediated superconductor, Phys. Rev. Lett. **114**, 157004 (2015).

[33] I. Errea, M. Calandra, and F. Mauri, First-principles theory of anharmonicity and the inverse isotope effect in superconducting palladium-hydride compounds, Phys. Rev. Lett. **111**, 177002 (2013).

[34] B. Rousseau and A. Bergara, Giant anharmonicity suppresses superconductivity in AlH_3 under pressure, Phys. Rev. B **82**, 104504 (2010).

[35] A. Meninno and I. Errea, *Ab initio* study of metastable occupation of tetrahedral sites in palladium hydrides and its impact on superconductivity, Phys. Rev. B **107**, 024504 (2023).

[36] D. Sun, V. S. Minkov, S. Mozaffari, Y. Sun, Y. Ma, S. Chariton, V. B. Prakapenka, M. I. Eremets, L. Balicas, and F. F. Balakirev, High-temperature superconductivity on the verge of a structural instability in lanthanum superhydride, Nat. Commun. **12**, 6863 (2021).

[37] I. A. Kruglov, A. V. Yanilkin, Y. Propad, A. B. Mazitov, P. Rachitskii, and A. R. Oganov, Crystal structure prediction at finite temperatures, npj Comput. Mater. **9**, 1 (2023).

[38] G. Dong, T. Cui, Z. Huo, Z. Liu, W. Chen, P. Hou, Y.-W. Fang, and D. Duan, Machine-learning potentials for quantum and anharmonic effects in superconducting $Fm\bar{3}m$ $LaBeH_8$, Mater. Today Phys. **59**, 101939 (2025).

[39] E. V. Podryabinkin, E. V. Tikhonov, A. V. Shapeev, and A. R. Oganov, Accelerating crystal structure prediction by machine-learning interatomic potentials with active learning, Phys. Rev. B **99**, 064114 (2019).

[40] Q. Tong, L. Xue, J. Lv, Y. Wang, and Y. Ma, Accelerating CALYPSO structure prediction by data-driven learning of potential energy surface, Faraday Discuss. **211**, 31 (2018).

[41] Z. Wang, X. Wang, X. Luo, P. Gao, Y. Sun, J. Lv, H. Wang, Y. Wang, and Y. Ma, Concurrent learning scheme for crystal structure prediction, Phys. Rev. B **109**, 094117 (2024).

[42] J. Wang, H. Gao, Y. Han, C. Ding, S. Pan, Y. Wang, Q. Jia, H.-T. Wang, D. Xing, and J. Sun, MAGUS: Machine learning and graph theory assisted universal structure searcher, Natl. Sci. Rev. **10**, nwad128 (2023).

[43] C. J. Pickard, Ephemeral data derived potentials for random structure search, Phys. Rev. B **106**, 014102 (2022).

[44] P. T. Salzbrenner, S. H. Joo, L. J. Conway, P. I. C. Cooke, B. Zhu, M. P. Matraszek, W. C. Witt, and C. J. Pickard, Developments and further applications of ephemeral data derived potentials, J. Chem. Phys. **159**, 144801 (2023).

[45] M. K. Bisbo and B. Hammer, Efficient global structure optimization with a machine-learned surrogate model, Phys. Rev. Lett. **124**, 086102 (2020).

[46] J. Pitfield, F. Brix, Z. Tang, A. M. Slavensky, N. Rønne, M.-P. V. Christiansen, and B. Hammer, Augmentation of universal potentials for broad applications, Phys. Rev. Lett. **134**, 056201 (2025).

[47] C.-N. Li, H.-P. Liang, S. Xu, H. Wang, B.-Q. Zhao, J. Yang, X. Zhang, Z. Lin, and S.-H. Wei, LoreX: A low-energy region explorer boosts efficient crystal structure prediction, J. Am. Chem. Soc. **147**, 9544 (2025).

[48] B. Deng, P. Zhong, K. Jun, J. Riebesell, K. Han, C. J. Bartel, and G. Ceder, CHGNet as a pretrained universal neural network potential for charge-informed atomistic modelling, Nat. Mach. Intell. **5**, 1031 (2023).

[49] I. Batatia, P. Benner, Y. Chiang, A. M. Elena, D. P. Kovács, J. Riebesell, X. R. Advincula, M. Asta, M. Avaylon, W. J. Baldwin, *et al.*, A foundation model for atomistic materials chemistry, J. Chem. Phys. **163**, 184110 (2025).

[50] H. Yang, C. Hu, Y. Zhou, X. Liu, Y. Shi, J. Li, G. Li, Z. Chen, S. Chen, C. Zeni, *et al.*, MatterSim: A deep learning atomistic model across elements, temperatures and pressures, arXiv:2405.04967.

[51] Y. Li, L. Wang, H. Liu, Y. Zhang, J. Hao, C. J. Pickard, J. R. Nelson, R. J. Needs, W. Li, Y. Huang, I. Errea, M. Calandra, F. Mauri, and Y. Ma, Dissociation products and structures of solid H_2S at strong compression, Phys. Rev. B **93**, 020103(R) (2016).

[52] I. Errea, M. Calandra, and F. Mauri, Anharmonic free energies and phonon dispersions from the stochastic self-consistent harmonic approximation: Application to platinum and palladium hydrides, Phys. Rev. B **89**, 064302 (2014).

[53] L. Monacelli, R. Bianco, M. Cherubini, M. Calandra, I. Errea, and F. Mauri, The stochastic self-consistent harmonic approximation: Calculating vibrational properties of materials with full quantum and anharmonic effects, J. Phys.: Condens. Matter **33**, 363001 (2021).

[54] K. Xia, H. Gao, C. Liu, J. Yuan, J. Sun, H.-T. Wang, and D. Xing, A novel superhard tungsten nitride predicted by machine-learning accelerated crystal structure search, Sci. Bull. **63**, 817 (2018).

[55] Y. Han, C. Ding, J. Wang, H. Gao, J. Shi, S. Yu, Q. Jia, S. Pan, and J. Sun, Efficient crystal structure prediction based on the symmetry principle, Nat. Comput. Sci. **5**, 255 (2025).

[56] https://github.com/microsoft/mattersim/ (2025).

[57] J. P. Perdew, K. Burke, and M. Ernzerhof, Generalized gradient approximation made simple, Phys. Rev. Lett. **77**, 3865 (1996).

[58] G. Kresse and J. Furthmüller, Efficient iterative schemes for *ab initio* total-energy calculations using a plane-wave basis set, Phys. Rev. B **54**, 11169 (1996).

[59] G. Kresse and J. Furthmüller, Efficiency of ab-initio total energy calculations for metals and semiconductors using a plane-wave basis set, Comput. Mater. Sci. **6**, 15 (1996).

[60] G. Kresse and D. Joubert, From ultrasoft pseudopotentials to the projector augmented-wave method, Phys. Rev. B **59**, 1758 (1999).

[61] R. Liu, E. Liu, J. Riebesell, J. Qi, S. P. Ong, and T. W. Ko, Matcalc: A python library for calculating materials properties from the potential energy surface (PES), https://github.com/materialsvirtuallab/matcalc (2024), version 0.0.4, BSD-3-Clause License, Released 2024-01-01.

[62] R. Bianco, I. Errea, M. Calandra, and F. Mauri, High-pressure phase diagram of hydrogen and deuterium sulfides from first principles: Structural and vibrational properties including quantum and anharmonic effects, Phys. Rev. B **97**, 214101 (2018).

[63] R. Caputo and A. Alavi, Where do the H atoms reside in PdH_x systems? Mol. Phys. **101**, 1781 (2003).

[64] A. Houari, S. F. Matar, and V. Eyert, Electronic structure and crystal phase stability of palladium hydrides, J. Appl. Phys. **116**, 173706 (2014).

[65] D. Long, M. Li, D. Meng, Y. He, I. T. Yoon, R. Ahuja, and W. Luo, Accounting for the thermo-stability of PdH_x ($x = 1$–3) by density functional theory, Int. J. Hydrogen Energy **43**, 18372 (2018).

[66] J. E. Worsham, M. K. Wilkinson, and C. G. Shull, Neutron-diffraction observations on the palladium-hydrogen and palladium-deuterium systems, J. Phys. Chem. Solids **3**, 303 (1957).

[67] H. Gao, Dateset of "Iterative learning scheme for crystal structure prediction with anharmonic lattice dynamics" [Data set], Zenodo (2006), 10.5281/zenodo.19348240